ROYAL SOCIETY
OF CHEMISTRY

PAPER

Check for updates

Pulsed-grown graphene for flexible transparent conductors†

Pramoda K. Nayak [ID] *

In the race to find novel transparent conductors for next-generation optoelectronic devices, graphene is supposed to be one of the leading candidates, as it has the potential to satisfy all future requirements. However, the use of graphene as a truly transparent conductor remains a great challenge because its lowest sheet resistance demonstrated so far exceeds that of the commercially available indium tin oxide. The possible cause of low conductivity lies in its intrinsic growth process, which requires further exploration. In this work, I have approached this problem by controlling graphene nucleation during the chemical vapor deposition process as well as by adopting three distinct procedures, including bis(trifluoromethanesulfonyl)amide doping, post annealing, and flattening of graphene films. Additionally, van der Waals stacked graphene layers have been prepared to reduce the sheet resistance effectively. I have demonstrated an efficient and flexible transparent conductor with the extremely low sheet resistance of 40 Ω sq^{-1}, high transparency (T_r ~90%), and high mechanical flexibility, making it suitable for electrode materials in future optoelectronic devices.

Introduction

The next-generation optoelectronic devices require materials with high mechanical flexibility, light weight, and high electrical conductivity and optical transparency to be used as electrodes.[1–4] Indium tin oxide (ITO) has been the most widely used transparent conductor in optoelectronic applications for over almost four decades. The sheet resistance (R_s) of ITO is thickness dependent and is found to be in the range of 5–60 Ω sq^{-1}, with the transmittance (T_r) of about 85–90% for 40–870 nm film thickness,[5] making it suitable for device applications. However, several drawbacks of ITO include the increased material cost, material deterioration due to ion diffusion, and brittleness, which limit its use in future flexible devices.[6,7] On the other hand, graphene is optically transparent, *i.e.*, each graphene layer has a very low opacity of 2.3%,[6,8] it is flexible[6,9] and it has high oxidation resistance,[10,11] making it an ideal candidate for transparent conducting films (TCFs).[12–15] Despite graphene's superior optical properties, flexibility, and relatively low manufacturing cost, the conductance of graphene sheets remains well below that of commercial ITO films.[16]

Department of Physics, Indian Institute of Technology Madras, Chennai 600036, India. E-mail: pnayak@iitm.ac.in

† Electronic supplementary information (ESI) available: Experimental details for the modified graphene growth, growth mechanism, experimental processes to reduce sheet resistance, graphene transfer process, sheet resistance measurement, flexibility test and reduction of sheet resistance in continuous flow graphene are given in Fig. S1–S7† and Table S1,† respectively. This material is available free of charge from the Royal Society of Chemistry (RSC) online library or from the author. See DOI: 10.1039/c8na00181b

Significant efforts have been made so far to reduce the R_s of graphene film by chemical doping,[17–19] substitutional doping,[20–22] or stacking of graphene films[7,23,24] in parallel while maintaining a high T_r to improve its potential to be harnessed in optoelectronic applications. Although chemical doping has been shown to effectively reduce the R_s of graphene down to 150 Ω sq^{-1} at T_r = 87%,[12] 125 Ω sq^{-1} at T_r = 97.4%,[13] and 80 Ω sq^{-1} at T_r = 80% for eight-layer stacked graphene,[7] the adsorption of moisture, other atoms, and molecules onto graphene after chemical treatment leads to the increase of R_s within few days.[25,26] Similarly, substitutional doping induces disorder in the graphene, thereby reducing its mobility as a result of scattering of Dirac electrons.[27,28] Additionally, most doping processes decrease the optical transparency of graphene film by changing its band structure or by forming optically reflective nanoparticles at the surface,[29,30] making it unsuitable for optoelectronic applications. Recently, a new growth technique has been introduced by Han *et al.*[31] which involves cyclic injection of carbon precursor (CH$_4$) during chemical vapor deposition (CVD) to suppress the multi-layer patches generally formed using continuous CH$_4$ flow, thereby improving both the optical and electrical performance of graphene. Similarly, other approaches, such as tri-fluoromethanesulfonimide (TFSA) doping,[19,32–34] post annealing,[35,36] and flattening of graphene films[37] have been carried out to reduce the R_s of graphene. However, no systematic study exists so far that combines all the aforementioned approaches, which is highly desired to achieve superior graphene film suitable for the transparent conducting electrode.

In the present work, I have prepared a high-quality graphene film using pulsed-grown technique and investigated its optical

and electrical performance using the combined effects of TFSA doping, stacking, post annealing and flattening. The prepared graphene film shows R_s of a few hundred Ω sq^{-1}, on/off ratio of $\sim$13, along with a high I_{2D}/I_G ratio (>1.5). TFSA doped four layer stacked graphene films show a low R_s of 40 Ω sq^{-1} and transmittance of 90%, which are almost comparable to those of ITO. The combination of TFSA doping, post annealing and flattening of graphene film is found to reduce the R_s by 80%, the highest value reported so far. Finally, the mechanical flexibility of this highly conducting and transparent film has been demonstrated, making it suitable for application as a flexible transparent conducting electrode.

Results and discussion

Growth of monolayer graphene on Cu substrate using CVD has been a well-established technique since 2009,[38–40] where the nucleation and growth of graphene usually occurs by exposure of the Cu surface to a hydrocarbon gas under atmospheric pressure, low pressure or ultra-high vacuum (UHV) conditions. However, the grain boundaries in such graphene films act as scattering centers for electron waves, limiting electron mobility.[41,42] To minimize the grain boundary effect, I have modified the graphene growth process by supplying CH$_4$ in short pulses[31] instead of the conventional continuous CH$_4$ flow during the CVD growth of graphene on Cu, as illustrated in Fig. 1. The details of the synthesis process are provided in

Fig. S1 (see ESI†). In the case of continuous CH$_4$ flow used in literature so far, the rate of nucleation is very high, which leads to high density of graphene nucleation seeds over the Cu surface.[43–47] These nucleation seeds interfere each other when growth persists, and hence, the graphene domains do not grow in the preferred orientation, and the average graphene domain size shrinks. On the other hand, in the pulsed-grown method, graphene domains are seen to coalesce in a preferred direction to form larger islands of $\sim$100 μm size (shown by arrows in Fig. S2 of ESI†). This provides evidence that the nucleation rate is expected to be slow in the pulsed-grown method, which leads to low density of graphene nucleation seeds. It can be noted that the preliminary annealing of the Cu substrate leads to a reconstruction of atomic distribution over the surface,[48] which causes directional growth of graphene domains, but not coalescence. As the Cu substrates used in this work were not pre-annealed, the directional growth due to substrate effect can be ruled out.

In addition to lower nucleation rate, the purpose of the pulsed CH$_4$ gas is to suppress carbon segregation at the defect sites in Cu, which aids in removing the multilayer patches generally formed using continuous CH$_4$ flow.[43] Moreover, the restoration time after each CH$_4$ pulse increases the catalytic activity of H$_2$ gas, during which hydrogen etches off the amorphous carbon atoms and the sp^3 carbon network present on the surface. Repeated alternating cycles of growth with CH$_4$ pulse and restoration of H$_2$ treatment promote the complete transformation of the carbon chain to a most stable sp^2 C–C network,
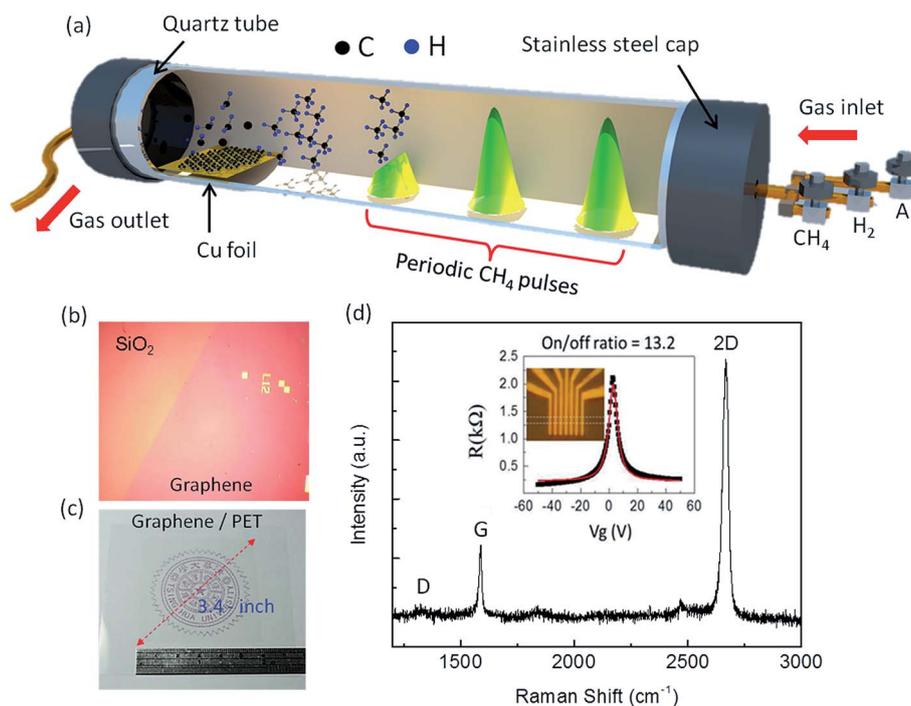

Fig. 1 (a) Schematic of the designed CVD system with introduction of periodic CH$_4$ pulses into the reaction zone. (b) OM image of pulse-grown graphene film transferred onto marked 300 nm SiO$_2$/Si substrate. The graphene film is clearly distinguishable from bare SiO$_2$ with the color contrast. (c) Camera image of 3.4-inch graphene film transferred onto 125 μm thick PET substrate. (d) Raman spectrum of transferred graphene film on SiO$_2$ substrate. Both G and 2D band peaks are very symmetric with full width at half maximum (FWHM) of 15 and 30 cm^{-1}, respectively. The I_{2D}/I_G intensity ratio is >1.5, which confirms that the prepared graphene is monolayer. A slight D band intensity is present in the Raman spectrum, which probably arises from the etching process. The inset shows the R vs. V_g plot for graphene-based FET in back-gate configuration.

as shown in Fig. S3 (ESI†). These hydrogen atoms not only promote the activation of physisorbed methane but also remove defects in carbon structures, which can be described in the following equation,

$$H_s + (graphene\text{-}defects) \Leftrightarrow (graphene\text{--}C) + (CH_x)_s \quad (1)$$
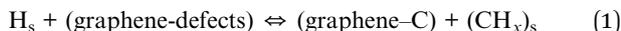
As a consequence, structural defects such as pentagon and heptagon structures are minimized, leading to a clean and defect-free graphene surface. The schematic illustration in Fig. S3a (see ESI†) shows the evolution of surface defects emerging from unexpected bumps, protrusions, and grooves on the surface; those bring up electron scattering issues in graphene, leading to Fermi velocity degradation. The dwell time of CH_4 pulses also affects graphene domain size, as shown in Fig. S2.† Longer dwell time of CH_4 pulses leads to a smaller graphene domain size of $\sim$2–3 μm (Fig. S2a and b†), whereas larger domain sizes of $\sim$20–30 μm could be achieved for shorter dwell time of CH_4 pulses, as shown in Fig. S2c and d.† The preferred orientations of graphene domains are marked with arrows in Fig. S2,† where these domains are merged together to form larger islands ($\sim$100 μm). The large graphene domain size along with the defect-free surface increases the mobility of the electrons, due to the low defect density and grain boundary effect,[31] thereby decreasing the R_s. The as-prepared graphene film was transferred onto 300 nm SiO_2/Si substrate using the conventional poly(methyl methacrylate) (PMMA)-based transfer process, as shown in Fig. S4 (see ESI†), similar to Lin *et al.*,[49] and the optical microscope (OM) image is shown in Fig. 1b. For electromechanical characterization, the graphene film was also transferred onto a flexible polyethylene terephthalate (PET) substrate, and the corresponding OM image is shown in Fig. 1c. The quality of our graphene film is reflected from the symmetric 2D peak, large I_{2D}/I_G ratio (>1.5) and absence of D peak measured from the Raman spectrum on SiO_2/Si substrate, as shown in Fig. 1d, which confirm that the prepared graphene is predominantly monolayer and defect free. Moreover, the R *vs.* V_g plot of the graphene-based field effect transistor (FET), shown inset in Fig. 1d, shows strong electron-hole symmetry, a narrow profile width ($\sim$5.5 V), and gate modulation (on/off ratio) of about 13.2, which are the characteristic features of high-quality graphene.[50,51]

Several methods have been perused in order to reduce the R_s of graphene, including doping with TFSA, post annealing, flattening and stacking of graphene films. The schematics of the above processes are mentioned in Fig. S5 (see ESI†), and the overall processes are summarized below.

The organic dopant TFSA is hydrophobic in nature and an excellent candidate for doping graphene due to its following advantages: effective electron-withdrawing ability, high transmittance, smooth surface, and superior environmental stability.[33] TFSA has been used as a p-type dopant in carbon nanotubes[52] and also in graphene.[19,33,34,53] TFSA, with a –NH group, easily loses a proton and transforms to TFSI upon accepting an electron from graphene, which is characteristic of a Brønsted acid.[54] When an electron is transferred from graphene to TFSA, a charge–transfer complex is formed according to eqn (2),

$$(CF_3SO_2)_2NH + Graphene \rightarrow$$
$$[(CF_3SO_2)_2N]^- + H^+ + Graphene^+ \quad (2)$$
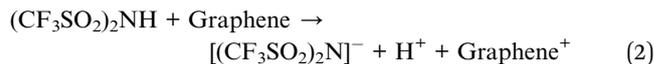
Thus, there is hole doping in the graphene that results in a shift of the Fermi level. In order to visualize this doping effect, I have performed electronic band structure calculation of TFSA-doped graphene using density functional theory (DFT), and the results are displayed in Fig. 2a and b. The details of DFT calculation are mentioned in the method section. Fig. 2a shows the optimized position of TFSA molecules absorbed on the surface of monolayer graphene. The constituent atoms of TFSA, such as N, S, O, C and F are marked in blue, yellow, red, grey and green, respectively. From the band structure result (Fig. 2b), the band gap value was found to be almost zero; *i.e.*, the gap between conduction band minimum (CBM) and valence band maximum (VBM) at the high-symmetry K point of the Brillouin zone and the Fermi level shifts below VBM, which is characteristic of p-doped graphene.[55,56] TFSA-doped graphene was prepared by spinning a few droplets of TFSA over graphene film at 3000 rpm for 30 s. The Raman spectra of pure and TFSA-doped graphene are shown in Fig. 2c. The characteristic Raman peaks for pristine graphene, located at 1588 cm^{-1} and 2669 cm^{-1}, correspond to G band (first-order Raman process) and 2D band (second-order Raman process), respectively.[57] Both pristine and TFSA-doped graphene exhibit very intense and symmetric 2D peaks with a large I_{2D}/I_G ratio (>1.5). Compared to pristine graphene, doped graphene shows a large blue shift for both G peak ($\Delta G = 6$ cm^{-1}) and 2D peak ($\Delta 2D = 33$ cm^{-1}), which confirms that there is charge transfer from graphene to TFSA, thereby causing p-doping,[58] which coincides with my calculation result. Interestingly, the D-peak, which corresponds to the TO phonons around the K point of the Brillouin zone and is the signature of defects on the graphene surface, is found to be absent before or after doping. This observation indicates that TFSA treatment is not destructive to the chemical bonds of graphene, which is quite similar to HNO$_3$-doped graphene.[18]

In the pursuit of transparent conducting applications, the optical and electrical properties of 1×1 cm^2 pristine and doped graphene films prepared by pulsed-grown method were analyzed, as shown in Fig. 3. The optical transmittance of the graphene films in the visible range was measured using an UV-VIS-NIR spectrophotometer (UV-3600, Shimadzu). For this measurement, graphene films were transferred on a cover glass as a single layer and as multiple stacked layers, and a bare cover glass was used as a reference. Multiple-layered "graphene stacks" were created using the transfer process sequentially. Fig. 3a depicts the wavelength dependence of the optical transparency of one- to four-layer-stacked pristine graphene films. The transmittance, T_r (%), of stacked graphene films at $\lambda = 550$ nm extracted from (a) was found to be 97.3, 94.6, 92.9 and 90 for one, two, three and four layers, respectively (Fig. 3b). Because each graphene layer has an opacity of 2.3%,[8] the transmittance decreases by $\sim$2.3% for each added layer, indicating that the film behaves as a set of individual graphene layers.[8,59] A slight variation in the transmittance values as per layer numbers predicted from theoretical calculation may be due to impurities present in the interface of the artificially built
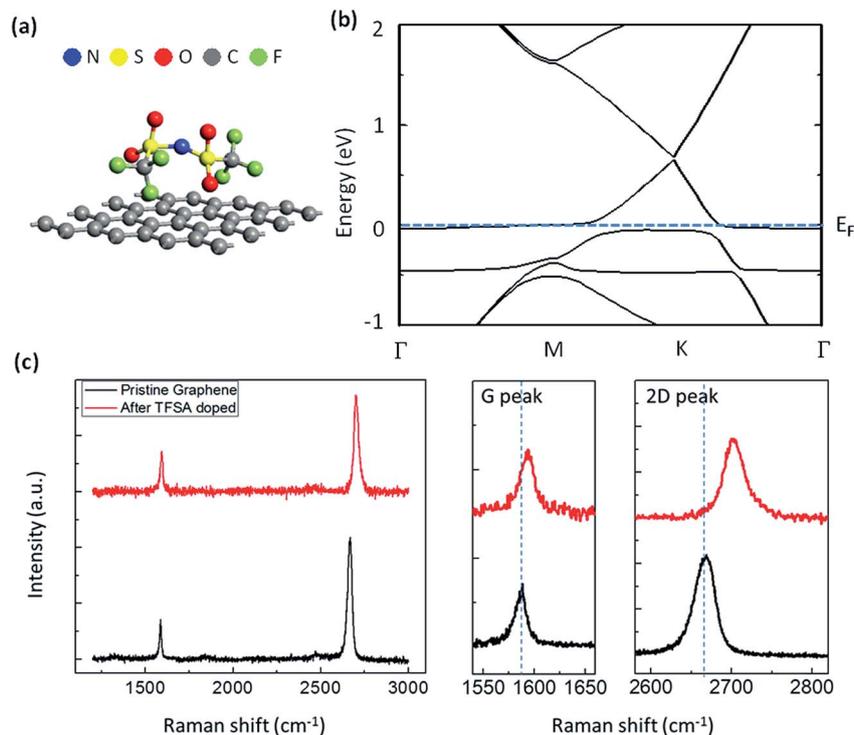
Fig. 2 Effect of TFSA doping on the Raman spectra of pulsed-grown graphene. (a) Optimized position of TFSA molecules absorbed on the surface of monolayer graphene. The constituent atoms of TFSA, such as N, S, O, C and F are marked in blue, yellow, red, grey and green, respectively. (b) Band structure calculation of TFSA-doped graphene using DFT. The band gap is almost zero; *i.e.*, the gap between conduction band minimum and valence band maximum at the high symmetry K point of the Brillouin zone and the Fermi level shifts below VBM due to p-doping. (c) Raman spectra of CVD graphene before and after TFSA doping. The G and 2D peaks of both the graphene films are extrapolated and plotted in separate panels for comparison. Compared to pristine graphene, doped graphene shows a large blue shift for both G peak ($\Delta G = 6$ cm^{-1}) and 2D peak ($\Delta 2D = 33$ cm^{-1}), which confirms that there is charge transfer from graphene to TFSA.

weak van der Waals stacked layers.[60] Similar behavior has also been observed by Karsy *et al.*[7] for stacked graphene layers. The evolution of graphene layers is also detectable from the change in color contrast observed from the optical images, as shown in the inset of Fig. 3b, which is minimum for one layer and maximum for four layers. The optical transmittance of TFSA-doped graphene also varies in a similar fashion to pristine graphene. For comparison, the optical transmittance of pristine and doped monolayer graphene is shown in Fig. 3c. It is observed that the T_r values of both films at $\lambda = 550$ nm are almost same, and hence, TFSA doping has no effect on the T_r of the graphene film. Fig. 3d shows the R_s of pristine and doped graphene films measured using van der Pauw method. The details of R_s measurement of graphene films are shown in Fig. S6 (see ESI†). In both the cases, R_s decreases with the increase in number of graphene layers. The R_s of monolayer graphene film is 288 Ω sq^{-1} with T_r of 97.3%, whereas that of four-layer graphene is 86 Ω sq^{-1}, while still maintaining a relatively high T_r of about 90%. Similarly, the R_s of doped graphene varies from 134 Ω sq^{-1} to a lowest value of 40 Ω sq^{-1} with the increase in number of graphene layers from one to four, while maintaining the same T_r values as those of pure graphene layers. In principle, the R_s of multilayer film, R_{sn}, is related to the R_s of one layer film, R_{s1}, by the relation $R_{sn} = R_{s1}/n$, where n is the number of graphene layers if all layers are acting

independently of each other. However, the average R_s of our films decreases slightly by stacking four graphene layers. The discrepancy might be explained by considering that the cracks in one film are bridged by its neighboring films, thus increasing the conductivity.[61] As stated earlier, when an electron is transferred from the graphene to TFSA, graphene becomes p-doped according to eqn (2). This results in a shift of the Fermi level (Fig. 3b), which increases the carrier concentration and thus the conductivity of the graphene layers. With the increase in layer numbers, there is further increment in the carrier concentration and density of states (DOS) at the Dirac point, which results in higher conductivity. This effect was first observed with single-walled carbon nanotubes (SWCNTs), where the doping of the SWCNTs with TFSA led to an increase in the conductivity of SWCNT films.[52] Since SWCNTs and graphene have essentially the same chemical structure, it is worth noting that TFSA doping yields lower sheet resistance.

Fig. 4a compares the sheet resistance of our graphene films prepared by pulsed-grown method with some others reported in literature as a function of T_r at $\lambda = 550$ nm. An extremely low R_s of 40 Ω sq^{-1} was observed for TFSA-doped four-layer stacked graphene films at a T_r of 90%. Such a low value of R_s is promising for designing an extremely efficient transparent conductor, and the T_r value is almost comparable with that of ITO.[62,63] The R_s of our pristine and TFSA-doped graphene films
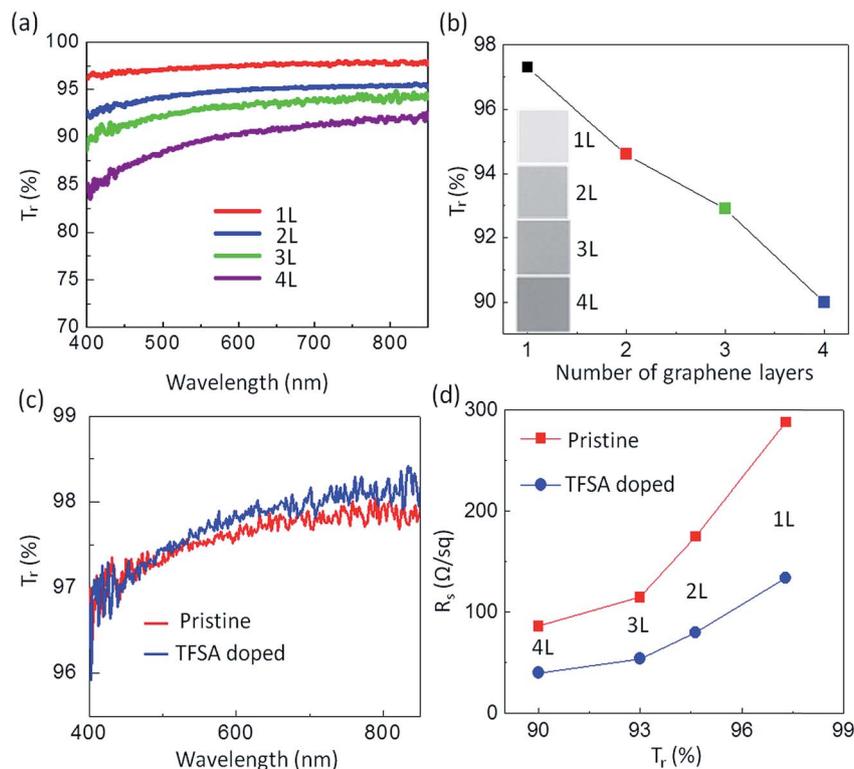
Fig. 3 Evaluation of pulsed-grown graphene films as transparent conductor. (a) Transmittance spectra of one- to four-layer stacked graphene films in the visible region of the energy spectrum. (b) T_r (%) as a function of the number of graphene layers extracted from (a) at $\lambda = 550$ nm. Inset shows photographs of stacked graphene layers. (c) Comparison of transmittance spectra between one-layer pristine graphene and TFSA-doped graphene. (d) R_s vs. T_r (%) of pristine and TFSA-doped graphene films for one to four stacked layers.

is very low compared to that of wet transferred graphene[61] and HNO$_3$-doped graphene.[60] However, these values are a little higher than the theoretical calculated values.[64] These higher experimental R_s values could be due to the presence of small metallic contaminants on the graphene surface during the transfer process. For the monolayer case, the R_s of prepared graphene films is also low compared to CHCl$_3$-doped graphene[24] and annealed and polished graphene,[65] but a little higher than KI-doped graphene.[66]

Besides TFSA doping (T), I carried out post annealing (A) and flattening (F) of graphene films to reduce the R_s, as shown in Fig. 4b. The maximum reduction in the R_s (ΔR_s) was observed for T (68%) compared to A (66%) and F (22%). Interestingly, the combination of all three effects ($T + A + F$) shows a maximum ΔR_s of 80%, whereas other combinations ($A + T$), ($F + T$) and ($A + F$) show ΔR_s of 79%, 70% and 64%, respectively. The above methods also have been applied to graphene prepared by continuous CH$_4$ flow in literature, including TFSA doping,[19,33,67] annealing,[35,36] and stacking,[7,23,24] as shown in ESI Table S1.† The reduction is R_s value is 30–75%, 7–30% and 50–58% for TFSA doping, annealing and stacking, respectively, which are comparatively less with reference to pulsed-grown graphene. During post annealing, the residual PMMA present on the surface of graphene decomposes at a temperature > 160 °C.[49] It is expected that the decomposition products of this molecule form cross links with the graphene surface by forming dangling bonds, and the surface absorbs O$_2$ or water vapor during

cooling to room temperature, becoming heavily p-doped, which leads to increased conductance. Flattening of graphene films was carried out using PMMA, in which the PMMA/graphene stack was prepared and heated at elevated temperatures (~150–160 °C). Heating of PMMA resulted in softening and expanding PMMA, allowing it to relax flat upon the substrate and thereby minimizing any wrinkling of the graphene, in turn restricting mechanical and electrical degradation, as reported by Goniszewski et al.[37] However, the effect of flattening was found to be very insignificant compared to TFSA doping and post annealing (Fig. 4b).

In addition to high optical T_r and low R_s, the graphene film should show excellent mechanical flexibility when used to make flexible and stretchable electrodes.[68] In order to investigate the mechanical flexibility of the present graphene films, the pristine as well as the doped monolayer graphene films were transferred onto a 125 µm thick polyethylene terephthalate (PET) substrate coated with a thin PDMS layer (Nan Ya Plastics Corporation, Taiwan (BH216)). Prior to graphene transfer, 30 nm SiO$_2$ was deposited on PET by E-gun evaporation technique to reduce its surface roughness. Fig. 5a shows the photograph of highly transparent graphene film transferred onto flexible PET substrate. To check the environmental stability of TFSA doping, the R_s of TFSA-doped graphene was measured for several days (Fig. 5b). Interestingly, there was no deterioration in R_s observed, even after 18 days, endorsing its superior environmental stability. Fig. 5c presents the R_s of pristine graphene film
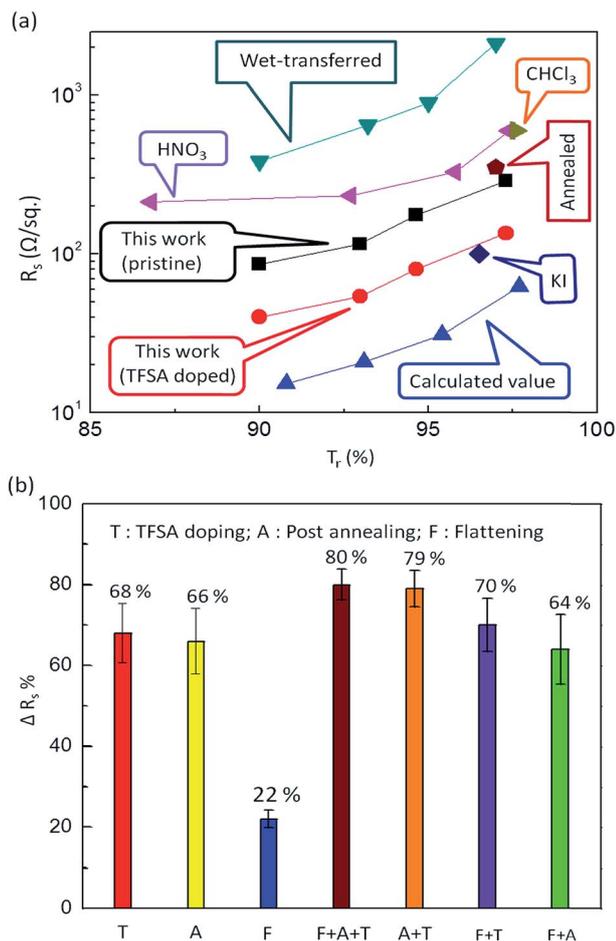
Fig. 4   (a) Comparison of R_s of the pulsed-grown graphene films with those reported in the literature as a function of T_r (%) at $\lambda = 550$ nm. An extremely low R_s of 40 Ω sq^{-1} was observed for TFSA-doped four-layer stacked graphene films at a T_r of 90%, which is almost comparable with that of ITO.[62,63] The R_s values of pristine (black squares) and TFSA-doped graphene films (red circles) of the present work are very low compared to those of wet transferred graphene (blue-green triangles)[61] and HNO$_3$ doped graphene (purple triangles).[60] However, these values are slightly higher than the theoretical calculated values.[64] For the monolayer case, the R_s of the present graphene films is also low compared to CHCl$_3$-doped graphene (olive-green triangle)[24] and annealed graphene (chocolate-brown pentagon),[65] but slightly higher than KI-doped graphene (blue diamond).[66] (b) Reduction in R_s (ΔR_s) of graphene films by TFSA doping (T), post annealing (A), flattening (F) and some combination of these processes. The maximum ΔR_s is 68% for TFSA doping compared to post annealing (66%) and flattening (22%). The combination of all three effects ($T + A + F$) shows maximum ΔR_s of 80%, whereas other combinations ($A + T$), ($F + T$) and ($A + F$) show ΔR_s of 79, 70 and 64%, respectively.

for bending-recovery cycles. For each cycle, graphene/PET was first bent to an angle of 162° (radius of curvature = 0.35 mm) with an interval of 18° and then fully relaxed in the subsequent interval. The schematic diagram of graphene/PET bending is shown in Fig. S7 (see ESI†). The arrows indicate the direction of bending and recovery. Prior to bending, the R_s of pristine graphene/PET was 419 Ω sq^{-1}, which is higher than the 288 Ω sq^{-1} observed for graphene/SiO$_2$, and this is probably due to the

high RMS surface roughness of PET (4.3 nm) compared to pure SiO$_2$ (1 nm). During bending, there was slight increase in the R_s, then it recovered after releasing the stress. This process was performed through the repeated bending and relaxing steps up to 100 cycles (Fig. 5d). Interestingly, the R_s remained unperturbed up to 100 bending cycles, which demonstrates the high flexibility of the prepared graphene film, similar to those observed by other groups.[69,70]

Bending of PET substrate produced surface strain on the graphene/PET film. The tensile strain was determined by the relatively extended length of graphene film upon bending of the underlying supporting PET substrate.[71] By assuming the length of the neutral axis of flat PET to be L_0, which changes with respect to the subsequent bending angle (θ), the bending radius (r) was calculated using $L_0 = r \times \theta$. Furthermore, the uniaxial tensile strain was calculated from the following relation,[72,73]

$$\varepsilon = \frac{100t}{(2r + t)}\%, \tag{3}$$

where t is the thickness of the PET substrate. Fig. 4c inset shows the relative change in R_s versus strain due to bending. At a maximum tensile strain of 1.77%, the R_s of the graphene film increased by 10–11%, which is much smaller than the 321% observed for ITO at 2.14% tensile strain.[74] Such a minor change in the R_s implies that the prepared graphene films are much more robust against bending and have advantages over ITO films in terms of superior mechanical flexibility.

Experimental

Modified graphene growth process

Graphene sheets used in the current study were grown by atmospheric pressure chemical vapor deposition (APCVD) on polycrystalline Cu foils, using methane (99.99%) as carbon source. Prior to growth, the Cu foils were cleaned with acetone and isopropyl alcohol (IPA) by sonication, followed by etching in acetic acid for 30 min to remove surface oxides. Then, the Cu foils were mounted in the CVD chamber, and graphene growth process was configured in several steps in the presence of steady flow of hydrogen and argon gas in the proportion of 10–20 : 300 sccm. The schematic of the growth process is shown in Fig. S1 (see ESI†). In the first step, the furnace was ramped up to 1050 °C over 40 min. In the second step, pre-annealing was carried out by holding the temperature at 1050 °C for 30 min. By this step, the oxide on the copper foil surface was being removed and the internal stress was released by recrystallization to make the surface of copper foil smoother. Then, methane with flow rate of <1 sccm was fed into the reaction chamber for 50 min (15–25 cycles) in step 3, during which graphene growth occurred. In each cycle, CH$_4$ pulse was given for 30 s and released for 1 min. This process was carried out by means of a control device, which controlled the import flow rate of the CH$_4$ gas by controlling the opening and closing of the gas valve. That is to say, the CH$_4$ supply during this reaction step was changed continuously (first increased and then decreased in one cycle), which is different from the constant gas supply process in prior literature. Finally, the Cu
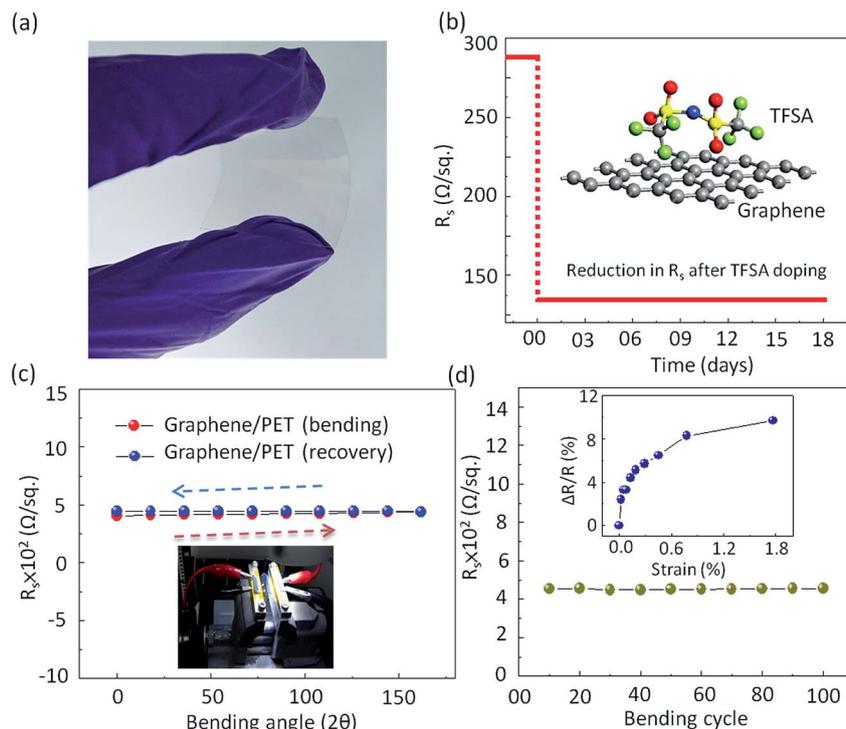
Fig. 5 Analysis of electromechanical properties of graphene films. (a) Photograph showing highly transparent graphene film transferred onto flexible PET substrate. (b) Reduction in R_s of graphene film after TFSA doping and its environmental stability test. The R_s remains preserved up to 18 days, revealing superior environmental stability. (c) The R_s vs. bending angle of pristine graphene measured on PET substrate under different bending conditions. The arrows show the direction of bending and recovery. Inset shows a photograph of the mechanical flexibility test setup. (d) The R_s vs. bending cycles for single-layer graphene/PET substrate. The R_s remains unperturbed up to 100 bending cycles. Inset shows the relative change in R_s versus strain due to bending. At a maximum tensile strain of 1.77%, the R_s of the graphene film increased by 10–11% only.

foils were moved to the cooling zone, which is equipped with a cooling system, in step 4.

Graphene transfer process using PMMA

Graphene layers on Cu foils were coated with 300 nm thick PMMA, followed by etching in a 16.5% aqueous hydrochloric acid solution. The PMMA film, along with the attached graphene, was detached from the metal substrate after a whole night. The PMMA/graphene film was then rinsed with DI water, transferred to a silicon or target substrate, and rinsed with warm acetone to remove the PMMA. Photographs of the graphene transfer process are shown in Fig. S4 (see ESI†).

Experimental methods to reduce sheet resistance

TFSA-doped graphene was prepared by spinning a few droplets of TFSA over graphene film at 3000 rpm for 30 s. Post annealing was carried out in two steps, first at 250 °C in air and then at 250 °C in the presence of mixed H_2 (200 sccm) and Ar (400 sccm) atmosphere for 2 h, similar to Lin et al.[49] Flattening of graphene film was performed by spin coating of PMMA at 3000 rpm for 30 s, followed by heating at elevated temperatures (~150–160 °C) and, finally, removing PMMA using warm acetone. Stacked graphene films were prepared by sequential transfer of one graphene layer over another, up to four layers. No adhesive was used at the interfaces, and the interlayer bonding is only due to van der Waals force.

Band structure calculation of TFSA-doped graphene

Band structure calculation was performed by placing the TFSA molecule on the top of single-layer graphene. The pseudopotential density functional SIESTA package was used for band structure calculations,[75,76] with the local density approximation (LDA) representing the exchange correlation potential[77,78] and with an energy mesh cutoff of 150 Ry. Optimization of initial experimental structures was performed using analytical energy gradient with respect to atomic coordinates and unit cell parameters. The structures were relaxed until the force on each atom was less than 0.01 eV Å^{-1}. The Brillouin zone was sampled with a grid of 5 × 5 × 1 k-points within the Monkhorst–Pack scheme.[79] Band structures were calculated along the high symmetry points using the path Γ–M–K–Γ.

Conclusions

In summary, high-quality graphene was prepared by supplying methane pulses instead of the conventional continuous methane flow used in CVD. The lowest sheet resistance of a few hundred Ω sq^{-1}, the on/off ratio of ~13 for the graphene-based FET, and the high I_{2D}/I_G ratio of >1.5 demonstrate the quantitative signatures of graphene quality. Several processes, including TFSA doping, post annealing, flattening and stacking of graphene films, were carried out in order to reduce the sheet resistance, making them suitable for application as transparent

conducting electrode. An extremely low sheet resistance of 40 Ω sq^{-1} for TFSA-doped four-layer stacked graphene films at a transmittance of 90% was reported, which is almost comparable with that of ITO. TFSA doping was found to be very effective for increasing the conductivity of graphene film. Interestingly, the combination of TFSA doping, post annealing and flattening of graphene films was found to reduce the sheet resistance by 80%, which is the highest value reported so far. Besides, the superior mechanical flexibility of this highly conducting and transparent film was also demonstrated, making it suitable as a transparent conducting electrode. This work provides a new pathway to obtain a suitable transparent conducting electrode for applications in various optoelectronic devices such as solar cells, touch screens, and transparent displays in the future.

Conflicts of interest

There are no conflicts to declare.

Acknowledgements

Notes and references

1 A. Kumar and C. Zhou, *ACS Nano*, 2010, **4**, 11–14.

2 D. S. Hecht, L. Hu and G. Irvin, *Adv. Mater.*, 2011, **23**, 1482–1513.

3 J. Du, S. Pei, L. Ma and H. M. Cheng, *Adv. Mater.*, 2014, **26**, 1958–1991.

4 J. Ning, L. Hao, M. Jin, X. Qiu, Y. Shen, J. Liang, X. Zhang, B. Wang, X. Li and L. Zhi, *Adv. Mater.*, 2017, **29**, 1605028.

5 H. Kim, J. S. Horwitz, G. Kushto, A. Piqué, Z. H. Kafafi, C. M. Gilmore and D. B. J. Chrisey, *J. Appl. Phys.*, 2000, **88**, 6021–6025.

6 L. G. De Arco, Y. Zhang, C. W. Schlenker, K. Ryu, M. E. Thompson and C. Zhou, *ACS Nano*, 2010, **4**, 2865–2873.

7 A. Kasry, M. A. Kuroda, G. J. Martyna, G. S. Tulevski and A. A. Bol, *ACS Nano*, 2010, **4**, 3839–3844.

8 R. R. Nair, P. Blake, A. N. Grigorenko, K. S. Novoselov, T. J. Booth, T. Stauber, N. M. R. Peres and A. K. Geim, *Science*, 2008, **320**, 1308.

9 X. Huang, T. Leng, M. Zhu, X. Zhang, J. Chen, K. Chang, M. Aqeeli, A. K. Geim, K. S. Novoselov and Z. Hu, *Sci. Rep.*, 2015, **5**, 18298.

10 S. Chen, L. Brown, M. Levendorf, W. Cai, S. Y. Ju, J. Edgeworth, X. Li, C. W. Magnuson, A. Velamakanni, R. D. Piner, J. Kang, J. Park and R. S. Ruoff, *ACS Nano*, 2011, **5**, 1321–1327.

11 P. K. Nayak, C. J. Hsu, S. C. Wang, J. C. Sung and J. L. Huang, *Thin Solid Films*, 2013, **529**, 312–316.

12 K. S. Kim, Y. Zhao, H. Jang, S. Y. Lee, J. M. Kim, K. S. Kim, J. H. Ahn, P. Kim, J. Y. Choi and B. H. Hong, *Nature*, 2009, **457**, 706–710.

13 J. B. Wu, M. Agrawal, H. A. Becerril, Z. N. Bao, Z. F. Liu, Y. S. Chen and P. Peumans, *ACS Nano*, 2010, **4**, 43–48.

14 T. Kobayashi, M. Bando, N. Kimura, K. Shimizu, K. Kadono, N. Umezu, K. Miyahara, S. Hayazaki, S. Nagai, Y. Mizuguchi, Y. Murakami and D. Hobara, *Appl. Phys. Lett.*, 2013, **102**, 023112.

15 A. Ford, *Graphene for Transparent Conductive Film Applications*, LAP LAMBERT Academic Publishing, 2016.

16 P. P. Edwards, A. Porch, M. O. Jones, D. V. Morgan and R. M. Perks, *Dalton Trans.*, 2004, 2995–3002.

17 K. K. Kim, A. Reina, Y. Shi, H. Park, L. J. Li, Y. H. Lee and J. Kong, *J. Nanotechnol.*, 2010, **21**, 285205.

18 S. Bae, H. Kim, Y. Lee, X. Xu, J. S. Park, Y. Zheng, J. Balakrishnan, T. Lei, H. R. Kim, Y. I. Song, Y. J. Kim, K. S. Kim, B. Özyilmaz, J. H. Ahn, B. H. Hong and S. Iijima, *Nat. Nanotechnol.*, 2010, **5**, 574–578.

19 X. Miao, S. Tongay, M. K. Petterson, K. Berke, A. G. Rinzler, B. R. Appleton and A. F. Hebard, *Nano Lett.*, 2012, **12**, 2745–2750.

20 J. O. Hwang, J. S. Park, D. S. Choi, J. Y. Kim, S. H. Lee, K. E. Lee, Y. H. Kim, M. H. Song, S. Yoo and S. O. Kim, *ACS Nano*, 2012, **6**, 159–167.

21 L. D. Arsié, S. Esconjauregui, R. S. Weatherup, X. Wu, W. E. Arter, H. Sugime, C. Cepek and J. Robertson, *RSC Adv.*, 2016, **6**, 113185–113192.

22 M. Kim, K. J. Kim, S. J. Lee, H. M. Kim, S. Y. Cho, M. S. Kim, S. H. Kim and K. B. Kim, *ACS Appl. Mater. Interfaces*, 2017, **9**, 701–709.

23 Y. Xu, H. Yu, C. Wang, J. Cao, Y. Chen, Z. Ma, Y. You, J. Wan, X. Fang and X. Chen, *Nanoscale Res. Lett.*, 2017, **12**, 254.

24 J. S. Choi, H. Choi, K. C. Kim, H. Y. Jeong, Y. J. Yu, J. T. Kim, J. S. Kim, J. W. Shin, H. Cho and C. G. Choi, *Sci. Rep.*, 2016, **6**, 24525.

25 B. Chandra, A. Afzali, N. Khare, M. M. El-Ashry and G. S. Tulevski, *Chem. Mater.*, 2010, **22**, 5179–5183.

26 C. Yan, K. S. Kim, S. K. Lee, S. H. Bae, B. H. Hong, J. H. Kim, J. H. Kim, H. J. Lee and J. H. Ahn, *ACS Nano*, 2012, **6**, 2096–2103.

27 F. Schedin, A. K. Geim, S. V. Morozov, E. W. Hill, B. Blake, M. I. Katsnelson and K. S. Novoselov, *Nat. Mater.*, 2007, **6**, 652–655.

28 K. Rakhimov, A. Chaves and P. Lambin, *Appl. Sci.*, 2016, **6**, 256–266.

29 A. Capasso, T. Dikonimos, F. Sarto, A. Tamburrano, G. De Bellis, M. S. Sarto, G. Faggio, A. Malara, G. Messina and N. Lisi, *Beilstein J. Nanotechnol.*, 2015, **6**, 2028–2038.

30 G. H. Kim and S. Jeong, *Sci. Rep.*, 2015, **5**, 11227.

31 Z. Han, A. Kimouche, D. Kalita, A. Allain, H. A. Tash, A. R. Plantey, L. Marty, S. Pairis, V. Reita, N. Bendiab, J. Coraux and V. Bouchiat, *Adv. Funct. Mater.*, 2014, **24**, 964–970.

32 Y. C. Lai, B. S. Wu, S. C. Yu, P. Yu and G. C. Chi, *IEEE Conf.*, 2013, 2436–2438.

33 S. Tongay, K. Berke, M. Lemaitre, Z. Nasrollahi, D. B. Tanner, A. F. Hebard and B. R. Appleton, *Nanotechnology*, 2011, **22**(1–6), 425701.

34 F. Bausi, A. Schlierf, E. Treossi, M. G. Schwab, V. Palermo and F. Cacialli, *Org. Electron.*, 2015, **18**, 53–60.

35 O. V. Tolochko, T. V. Larionova, T. S. Koltsova, M. V. Kozlova, E. V. Bobrynina, O. A. Martynova and V. E. Gasumyants, *J. Phys.: Conf. Ser.*, 2017, **816**, 012012.

36 W. Choi, Y. S. Seo, J. Y. Park, K. B. Kim, J. Jung, N. Lee and Y. Seo, *IEEE Trans. Nanotechnol.*, 2015, **14**, 70–74.

37 S. Goniszewski, J. Gallop, M. Adabi, K. Gajewski, E. Shaforost, N. Klein, A. Sierakowski, J. Chen, Y. Chen, T. Gotszalk and L. Hao, *IET Circuits, Devices Syst.*, 2015, **9**, 420–427.

38 X. Li, W. Cai, J. An, S. Kim, J. Nah, D. Yang, R. Piner, A. Velamakanni, I. Jung, E. Tutuc, S. K. Banerjee, L. Colombo and R. S. Ruoff, *Science*, 2009, **324**, 1312.

39 Y. C. Lin, C. H. Jin, J. C. Lee, S. F. Jen, K. Suenaga and P. W. Chiu, *ACS Nano*, 2011, **5**, 2362–2368.

40 X. Li, L. Colombo and R. S. Ruoff, *Adv. Mater.*, 2016, **28**, 6247–6252.

41 H. S. Song, S. L. Li, H. Miyazaki, S. Sato, K. Hayashi, A. Yamada, N. Yokoyama and K. Tsukagoshi, *Sci. Rep.*, 2012, **2**, 337.

42 V. Kochat, C. S. Tiwary, T. Biswas, G. Ramalingam, K. Hsieh, K. Chattopadhyay, S. Raghavan, M. Jain and A. Ghosh, *Nano Lett.*, 2016, **16**, 562–567.

43 G. H. Han, F. Günes, J. J. Bae, E. S. Kim, S. J. Chae, H. J. Shin, J. Y. Choi, D. Pribat and Y. H. Lee, *Nano Lett.*, 2011, **11**, 4144–4148.

44 Y. Ogawa, K. Komatsu, K. Kawahara, M. Tsuji, K. Tsukagoshi and H. Ago, *Nanoscale*, 2014, **6**, 7288–7294.

45 H. Zhou, W. J. Yu, L. Liu, R. Cheng, Y. Chen, X. Huang, Y. Liu, Y. Wang, Y. Huang and X. Duan, *Nat. Commun.*, 2013, **4**, 2096.

46 L. P. Biŕo and P. Lambin, *New J. Phys.*, 2013, **15**, 035024.

47 X. Chen, L. Zhang and S. Chen, *Synth. Met.*, 2015, **210**, 95–108.

48 I. V. Antonova, *Phys.-Usp.*, 2013, **183**, 1115–1122.

49 Y. C. Lin, C. C. Lu, C. H. Yeh, C. Jin, K. Suenaga and P. W. Chiu, *Nano Lett.*, 2012, **12**, 414–419.

50 T. J. Ha, J. Lee, D. Akinwande and A. Dodabalapur, *IEEE Electron Device Lett.*, 2013, **34**, 559–561.

51 J. W. Suk, W. H. Lee, J. Lee, H. Chou, R. D. Piner, Y. Hao, D. Akinwande and R. S. Ruoff, *Nano Lett.*, 2013, **13**, 1462–1467.

52 S. M. Kim, Y. W. Jo, K. K. Kim, D. L. Duong, H. J. Shin, J. H. Han, J. Y. Choi, J. Kong and Y. H. Lee, *ACS Nano*, 2010, **4**, 6998–7004.

53 D. Kim, D. Lee, Y. Lee and D. Y. Jeon, *Adv. Funct. Mater.*, 2013, **23**, 5049–5055.

54 M. A. B. H. Susan, A. Noda, S. Mitsushima and M. Watanabe, *Chem. Commun.*, 2003, 938–939.

55 M. Pykal, P. Jurečka, F. Karlický and M. Otyepka, *Phys. Chem. Chem. Phys.*, 2016, **18**, 6351–6372.

56 B. J. Schultz, R. V. Dennis, V. Lee and S. Banerjee, *Nanoscale*, 2014, **6**, 3444–3466.

57 A. C. Ferrari, J. C. Meyer, V. Scardaci, C. Casiraghi, M. Lazzeri, F. Mauri, S. Piscanec, D. Jiang, K. S. Novoselov, S. Roth and A. K. Geim, *Phys. Rev. Lett.*, 2006, **97**, 187401.

58 R. Parret, M. Paillet, J. R. Huntzinger, D. Nakabayashi, T. Michel, A. Tiberj, J. L. Sauvajol and A. A. Zahab, *ACS Nano*, 2013, **7**, 165–173.

59 P. Blake, P. D. Brimicombe, R. R. Nair, T. J. Booth, D. Jiang, F. Schedin, L. A. Ponomarenko, S. V. Morozov, H. F. Gleeson, E. W. Hill, A. K. Geim and K. S. Novoselov, *Nano Lett.*, 2008, **8**, 1704–1708.

60 G. Gao, W. Gao, E. Cannuccia, J. T. Tijerina, L. Balicas, A. Mathkar, T. N. Narayanan, Z. Liu, B. K. Gupta, J. Peng, Y. Yin, A. Rubio and P. M. Ajayan, *Nano Lett.*, 2012, **12**, 3518–3525.

61 X. Li, Y. Zhu, W. Cai, M. Borysiak, B. Han, D. Chen, R. D. Piner, L. Colombo and R. S. Ruoff, *Nano Lett.*, 2009, **9**, 4359–4363.

62 H. Kim, J. S. Horwitz, G. P. Kushto, Z. H. Kafafi and D. B. Chrisey, *Appl. Phys. Lett.*, 2001, **79**, 284.

63 F. L. Wong, M. K. Fung, S. W. Tong, C. S. Lee and S. T. Lee, *Thin Solid Films*, 2004, **466**, 225–230.

64 F. Bonaccorso, Z. Sun, T. Hasan and A. C. Ferrari, *Nat. Photonics*, 2010, **4**, 611–622.

65 J. K. Lee, C. S. Park and H. Kim, *RSC Adv.*, 2014, **4**, 62453–62456.

66 M. Kim, A. Shah, C. Li, P. Mustonen, J. Susoma, F. Manoocheri, J. Riikonen and H. Lipsanen, *2D Mater.*, 2017, **4**, 035004.

67 Y. C. Lai, B. S. Wu, S. C. Yu, P. Yu and G. C. Chi, *IEEE Conf.*, 2013, 2436–2438.

68 C. Lee, X. Wei, J. W. Kysar and J. Hone, *Science*, 2008, **321**, 385–388.

69 L. G. De Arco, Y. Zhang, C. W. Schlenker, K. Ryu, M. E. Thompson and C. Zhou, *ACS Nano*, 2010, **4**, 2865–2873.

70 Z. Yin, S. Sun, T. Salim, S. Wu, X. Huang, Q. He, Y. M. Lam and H. Zhang, *ACS Nano*, 2010, **4**, 5263–5268.

71 T. Yu, Z. Ni, C. Du, Y. You, Y. Wang and Z. Shen, *J. Phys. Chem. C*, 2008, **112**, 12602–12605.

72 S. Takamatsu, T. Takahata, M. Muraki, E. Iwase, K. Matsumoto and I. Shimoyama, *J. Micromech. Microeng.*, 2010, **20**(1–6), 075017.

73 N. Lu, C. Lu, S. Yang and J. Rogers, *Adv. Funct. Mater.*, 2012, **22**, 4044–4050.

74 S. Lee, K. Lee, C. H. Liu and Z. Zhong, *Nanoscale*, 2011, **4**, 639–644.

75 Quantum Wise A/S, *Atomistix Tool Kit*, 2010, ch. 10.8.2.

76 M. Brandbyge, J. Mozos, P. Ordejon, J. Taylor and K. Stokbro, *Phys. Rev. B*, 2002, **65**, 165401.

77 D. M. Ceperley and B. J. Alder, *Phys. Rev. Lett.*, 1980, **45**, 566.

78 J. P. Perdew and A. Zunger, *Phys. Rev. B*, 1981, **23**, 5048.

79 H. J. Monkhorst and J. D. Pack, *Phys. Rev. B*, 1976, **13**, 5188.